ChemMedChem

Review
doi.org/10.1002/cmdc.202200004

Chemistry
Europe
European Chemical
Societies Publishing

www.chemmedchem.org

Recent Developments in Porous Silicon Nanovectors with Various Imaging Modalities in the Framework of Theranostics

Jing Qian,[a, b] Huang Wen,[a] Konstantin Tamarov,[a] Wujun Xu,*[a] and Vesa-Pekka Lehto*[a]

The number of *in vitro*, *ex vivo*, and *in vivo* studies on porous silicon (PSi) nanoparticles for biomedical applications has increased extensively over the last decade. The focus of the reports has been on the carrier properties of PSi concerning the therapeutic aspect due to several beneficial nanovector characteristics including high payload capacity, biocompatibility, and versatile surface chemistry. Recently, increasing attention has been paid to the diagnostic aspects of PSi, which is typically attributed to the biotraceability of the nanovector. Also, PSi has been studied as a contrast agent. When both these aspects, therapy and diagnosis, are integrated into one nanovector, we can discuss a real nanotheranostics approach. Herein, we review the recent progress developing PSi for various imaging modalities, specifically focusing on optical imaging, magnetic resonance imaging, and nuclear medicine imaging. Furthermore, we summarized the knowledge gaps that must be covered before applying PSi in clinical imaging, highlighting future research trends.

1. Introduction

Bioimaging is a useful tool for visualizing the biological structures of cells and tissues *in vitro* and *in vivo*.[1] It has become an indispensable method for doctors to accurately identify diseased tissues and monitor therapy responses from physiological and pathological changes.[2] Up to now, several bioimaging modalities, such as ultrasound,[3] X-ray,[4] nuclear medicine imaging (NMI),[5] and magnetic resonance imaging (MRI),[6] have been widely applied in clinical diagnosis. Due to the blossom of computer-assisted digital imaging and analysis, it is increasingly common to use these imaging modalities to guide therapy *in situ* and predict therapy outcomes.

With traditional clinical regimens, imaging contrast agents (CAs) and medicines are administered separately.[7] Thus, inconsistent information to monitor therapy is often provided with traditional imaging because imaging contrast and medicines are based on different platforms and have different pharmacokinetics and biodistributions *in vivo*. Diverse tools to integrate imaging and therapy into one nanovector have been provided with the nanotechnology development, i.e., to realize real nanotheranostics.[2b,8] In this context, an imaging modality may provide real-time feedback to monitor the therapy response because the contrast agent and therapeutic agent are inseparable and delivered in the same target site.[9] Moreover, other functions, such as targeting, can be endowed to the nanoparticles (NPs) via surface functionalization.[10] Thus, this type of 'all-in-one' nanovector enhances the advancement of biomedical engineering with better therapeutic outcomes and decreased side effects.[11] Up to now, many nanocarriers have been studied as the platform for theranostics, including polymeric colloidal NPs,[12] liposome NPs,[13] mesoporous NPs,[10,14] and iron oxide NPs.[15]

Porous silicon nanoparticles (PSiNPs) have been widely studied for different biomedical applications due to their attractive features.[16] First, they are biodegradable. The degradation product silicic acid is non-toxic and is essential for bone and collagen growth.[17] Second, unlike most polymeric biomaterials, the surface of PSiNPs can be easily modified through simple chemical treatments without affecting their overall performance.[18] Third, PSiNPs have a high surface area and large pore volume, enabling them to carry drugs, imaging agents, or both.[19] Fourth, with PSiNPs, the stability of the loaded agents can be enhanced due to the confined effect of the rigid porous framework. For example, the photostability of fluorescein isothiocyanate (FITC) was significantly enhanced after being loaded into PSi.[20]

In this minireview, the progress in develop PSi-based biological imaging approaches, including optical imaging, MRI, positron emission tomography (PET) and single-photon emission computed tomography (SPECT) imaging, is summarized. We also review the latest PSi-based imaging research in nanomedical applications especially pinpointing the promising prospects in guided drug delivery and cancer theranostics.

[a] J. Qian, H. Wen, K. Tamarov, W. Xu, Prof. V.-P. Lehto
Department of Applied Physics,
University of Eastern Finland
Yliopistonranta 1, 70211 Kuopio (Finland)
E-mail: vesa-pekka.lehto@uef.fi
wujun.xu@uef.fi
[b] J. Qian
College of Chemistry and Chemical Engineering,
Lanzhou University, Lanzhou 730000 (China)

ChemMedChem

Review
doi.org/10.1002/cmdc.202200004

Chemistry Europe
European Chemical
Societies Publishing

2. Imaging Models

PSi is widely used in various imaging modalities with different performances in sensitivity and spatial resolution (Table 1).[21] Optical imaging is an imaging technique that uses visible light, typically infrared in vivo, to detect various tissues and smaller objects. With optical CAs, different organelles in cells may be distinguished *in vitro* because of its remarkable sensitivity, thereby monitoring physiological activities at the cell level.[22] Fluorescence and photoluminescence-based optical imaging systems have the advantages of low cost, high-resolution, non-invasive, non-ionizing real-time imaging, which are undoubtedly the most cost-effective modality for cancer research. However, the barriers to tissue autofluorescence and limited tissue penetration prohibit their broad preclinical and clinical applications.[23] MRI is an imaging technique based on the basic principles of nuclear magnetic resonance.[24] High-resolution images with soft tissue contrast and quantitative assessment of the disease may be obtained with MRI.[25] Although MRI has an exceptional spatial resolution, its low sensitivity, expensive cost, slow data collection, and high CA toxicity are the main disadvantages hindering its wide clinical applications.[21c] NMI is a non-invasive imaging technique that includes PET and SPECT.[26] PET imaging is widely used in drug development, evaluation, and cancer diagnosis to provide critical anatomy, pharmacology, and pathology information.[27] Unlike PET imaging, SPECT imaging is performed by detecting single photons of different energies emitted by the radiotracer. Both PET and SPECT are more sensitive than MRI, and PET is known to have the highest sensitivity of all *in vivo* imaging techniques. However, low spatial resolution and radiation risk are the main disadvantages of these two technologies.[16c] Recent progresses regarding the application of PSi in optical imaging, NMI, and MRI are summarized in Table S1 (Supporting information). In the following chapters, the representative examples of the latest advances are discussed in detail, especially regarding theranostics and drug delivery.

2.1. Optical Imaging

Optical imaging is a relatively affordable and straightforward method for biomedical imaging compared with other imaging techniques, such as CT and MRI. Furthermore, nonionizing radiation is used to excite optical CAs, indicating an excellent safety of the imaging modality.[28] The ideal optical CA should have the following characteristics: (1) high fluorescence quantum yield, (2) good biocompatibility, (3) excellent photostability, and (4) precise targeting of specific tissues. Near-infrared (NIR) emission has deeper tissue penetration and causes less tissue damage than visible light, enhancing the signal-to-noise ratio and spatial resolution.[29] Thus, we focus on applying PSiNPs in NIR optical imaging in this review.

PSiNPs have been applied as carriers for NIR probes because of their high surface area and large pore volume.[30] The Cunin group successfully constructed multifunctional PSiNPs to deliver Ru(II)-complex photosensitizers for NIR imaging and photodynamic therapy (PDT).[31] The NPs were modified with mannose
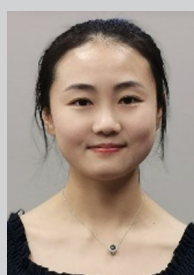
Jing Qian obtained her bachelor's degree from the Northeast Forestry University in 2016. She is currently a Joint Training PhD student at Lanzhou University and the University of Eastern Finland under the guidance of professor Vesa-Pekka Lehto. Her research interests focus on the synthesis of fluorescent and photoluminescent materials for early detection of disease markers.
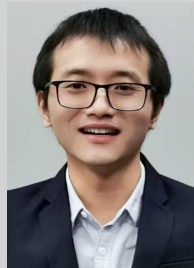
Huang Wen started in 2020 as a PhD student in the Pharmaceutical Physics Group in the Department of Applied Physics at the University of Eastern Finland. He received a master's degree in inorganic chemistry from the College of Chemistry and Chemical Engineering, Lanzhou University in 2018. His research goal is to design functional nano-silicon-based biomaterials for potential biomedical therapy and imaging.
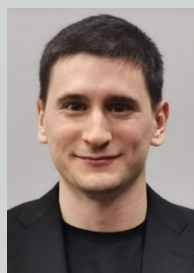
Konstantin Tamarov obtained a PhD in Applied Physics in 2017 and has worked as a postdoctoral researcher in the Department of Applied Physics at the University of Eastern Finland since 2018. His research interests include controlled photothermal therapy, electroless etching of Si, spin dynamics, and hyperpolarization of Si nanoparticles.

Wujun Xu is an Adjunct Professor in the Department of Applied Physics, University of Eastern Finland. He obtained a doctoral degree in Materials Science in 2008 from the University of Chinese Academy of Sciences. His research interests are in the synthesis and functionalization of porous nanomaterials for various biomedical applications, such as delivery of poorly soluble drugs, biomimetic nanomedicines, and light-triggered imaging and therapy.

Vesa-Pekka Lehto received his PhD from the University of Turku, Finland, in 1999. He currently holds a professorship in Materials Physics at the University of Eastern Finland where he started in 2008. He has published >200 refereed scientific journal papers. His h-index is 41 with a total number of >6000 citations (WoS). His resent research interests include the development of nanoporous drug carriers, the development of nanostructured silicon for metal adsorption, and the development of anode material based on nanostructured silicon for Li-ion batteries.

ChemMedChem

Review
doi.org/10.1002/cmdc.202200004

Chemistry
Europe
European Chemical
Societies Publishing

Table 1. Characteristics of some imaging modalities.[21]

| Imaging modality	Sensitivity (mol/L)	Spatial resolution	Merit	Shortcoming
NIR imaging	10^{-15}–10^{-17}	3–5 mm	High sensitivity	Low resolution Limited depth (<5 cm)
MRI	10^{-3}–10^{-5}	25–100 μm	High resolution	Low sensitivity high cost
PET	10^{-11}–10^{-12}	1–2 mm	High sensitivity	Low resolution high cost
SPECT	10^{-10}–10^{-11}	1–2 mm	High sensitivity	Low resolution high cost

for cancer targeting and polyethylene glycol (PEG) for improved biocompatibility. Powerful NIR imaging capability and efficient inhibition of cell growth were observed *in vitro* under NIR irradiation.

On the other hand, PSiNPs can be employed as imaging CAs without being labeled with fluorescent dyes or quantum dots because PSi itself possesses tunable photoluminescence in the range from visible light to NIR.[34] In addition, the photoluminescence of PSiNPs is more stable than the fluorescence from dyes, which can easily be photobleached.[34a,35] The Zabotnov group used picosecond laser ablation of porous silicon films and nanowires to synthesize small silicon nanoparticles (14–65 nm), which have fluorescence emission in the NIR range (600–1000 nm) and created a new prospect used as optical imaging contrast agents.[32] In addition, they can be used in OCT imaging (Figure 1A–D). The drawbacks of single-imaging modalities often limit their applicability, so multimodality i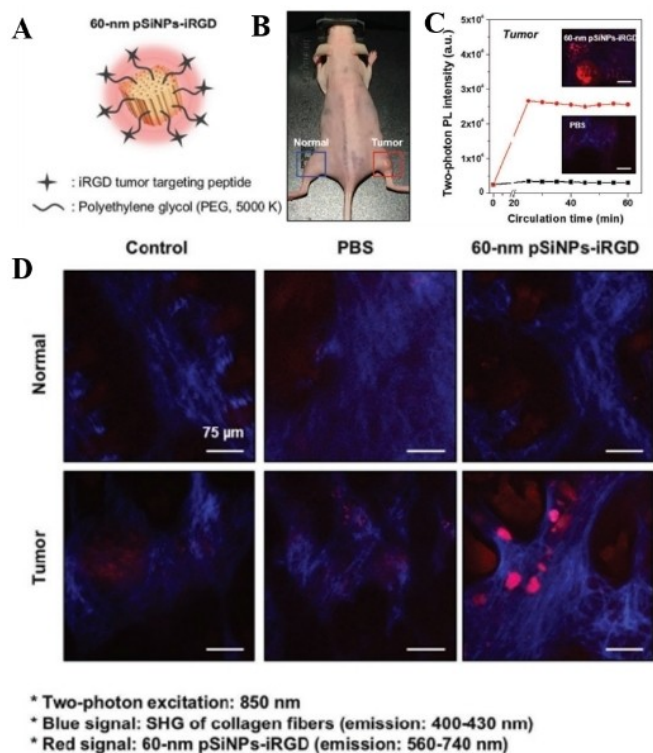maging has emerged. In 2017, Xia et al. fabricated PSiNPs@Fe$_3$O$_4$ nanocomposites for dual-mode imaging by covalently bonding superparamagnetic Fe$_3$O$_4$ NPs to photoluminescent PSiNPs.[33] In this nanocomposite, PSiNPs act as the NIR imaging agent, and Fe$_3$O$_4$ NPs were the CAs for MRI (Figure 1E–G). The nanocomposite had excellent biocompatibility, and it performed well in fluorescence/magnetic resonance bimodal imaging of cells *in vitro* and tumors *in vivo*.

The lifetime of microsecond-level photoluminescence is a unique feature of PSiNPs that can be used in biological imaging. Because of this long response time, the photoluminescence of PSiNPs can be distinguished temporally from the autofluorescence of living tissues, and this improves the resolution of spatial imaging.[36] The Sailor group prepared PEG-coated PSiNPs, and they used a commercial imaging system to evaluate the intensity and lifetime of fluorescence from NPs.[37] The results showed that PEG-PSiNPs can be successfully applied to time-gated (TG) imaging *in vivo*, as the interference from the short-lifetime fluorescence signal from the tissue autofluorophores was almost completely eliminated. With a delay of 25 ns, the signal-to-noise ratio with PSiNPs increased by 20-fold *in vivo*. However, the imaging contrast was much lower than the theoretical prediction in the commercial animal imaging system because of the fixed repetition rate of the pulsed laser and the relatively short delay time. Therefore, a specific system was designed for the microsecond domain of PSiNPs TG imaging, and it obtained a photoluminescence attenuation of about 500 μs (Figure 2).[38] When tracking the *in vivo* fate of target NPs relative to steady-state imaging, the signal-to-noise ratio was significantly improved compared to previous work (more than 100-fold). In addition, a light-emitting diode can be used as a source of excitation instead of a pulsed laser, providing a convenient and low-cost imaging system.

Although NIR imaging greatly improves the shortcomings of optical CAs in terms of limited tissue penetration and spatial resolution, there are still huge challenges for imaging CAs *in vivo*.[31] Unlike fluorescent molecules or atoms that absorb only one photon at a time in ordinary optical imaging, two-photon imaging means the fluorescent molecules being able to absorb two photons simultaneously under strong light excitation. Consequently, the two-photon microscopy has a higher signal-to-noise ratio, deeper penetration, higher spatial resolution, and it causes less damage to biological tissues than single-photon microscopy.[39] Kim reported iRGD-PEG modified PSiNPs for two-photon imaging of live animals. The intensity of photoluminescence and signal-to-noise ratio of the two-photon
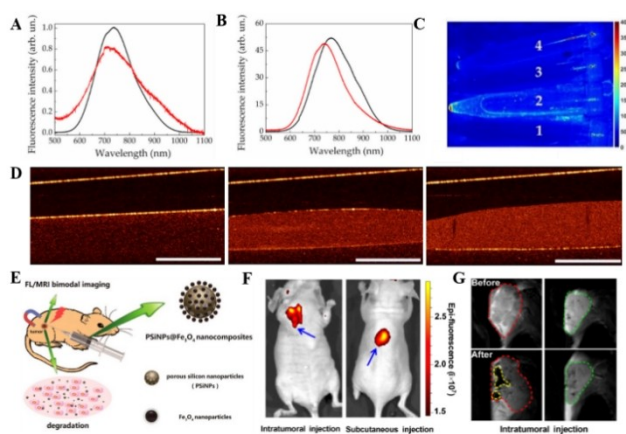
Figure 1. Fluorescence spectra of the initial SiNW arrays (black lines) of A) low- and B) heavily doped Si and corresponding SiNP suspensions (red lines). C) Fluorescence image of SiNP suspensions fabricated by low-doped SiNWs in water 1) and ethanol 2) and heavily-doped SiNWs in water 3) and ethanol 4); D) optical coherence tomography (OCT) images of agar gel phantoms without nanoparticles (left), with the SiNP suspension in water (middle) and ethanol (right).[32] Adapted with permission from Ref. [32], Copyright 2020, CC by License 4.0. E) Graphic abstract of multimodality imaging work showing the composition of nanomaterials and the scheme of the experiment *in vivo*; F) Fluorescent images of a tumor-bearing nude mouse after intratumoral and subcutaneous injections of oxidized PSiNPs@Fe$_3$O$_4$. G) MRI images of the mice after an intratumoral injection.[33] Adapted with permission from Ref. [33]. Copyright 2017 American Chemical Society.

ChemMedChem

Review
doi.org/10.1002/cmdc.202200004

**Chemistry
Europe**
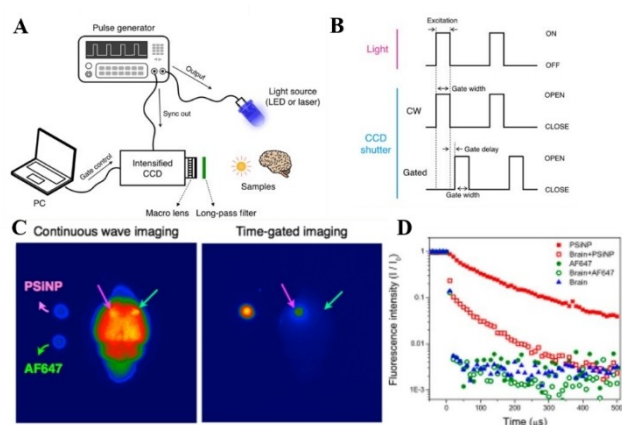European Chemical
Societies Publishing

Figure 2. A) Schematic diagram of the TG fluorescence imaging instrument. B) Notional waveforms of laser, continuous wave (CW), and TG fluorescence imaging. C) CW and TG fluorescence imaging of mouse brain before and after locally injected PSiNPs and AF647 (a fluorescent dye). D) Normalized intensity of the attenuation of the photoluminescence/fluorescence signal after the excitation pulse.[38] Adapted with permission from Ref. [38]. Copyright 2015 American Chemical Society.

Figure 3. A) Schematic illustration of the 60-nm PSiNP-iRGD. B) Photograph of xenograft tumor in the hind limb of a mouse under ambient light. C) Intensity of signals from two-photon microscopy for normal (blue box, left) and tumor (red box, right) regions of a xenograft tumor in the hind limb of a mouse. D) Two-photon microscopy images of sections from normal and tumor regions post-injection of either PBS or 60-nm PSiNP-iRGD for 1 h.[40] Adapted with permission from Ref. [40]. Copyright 2017 WILEY-VCH Verlag GmbH & Co. KGaA, Weinheim.

imaging of the NPs was significantly improved by increasing the two-photon absorption cross-section by restricting the size of PSINPs to 60 nm (Figure 3).[40] In addition, the tumor-targeting effect of 60-nm PSiNPs-iRGD was confirmed by the mouse orthotopic HeLa tumor model experiment (Figure 3D).

In general, PSi-based nanosystems have great potential in bioimaging, as the long-lived photoluminescence emission can be employed to eliminate the interference of tissue autofluorescence. This enhanced the discrimination of the CA from the endogenous fluorophores of living tissues. In addition, two-photon imaging also effectively improves spatial resolution. Combined with the other attractive features, such as high surface area and good biocompatibility, the unique photoluminescence of PSINPs forms the basis for the next generation optical imaging-based theranostic.

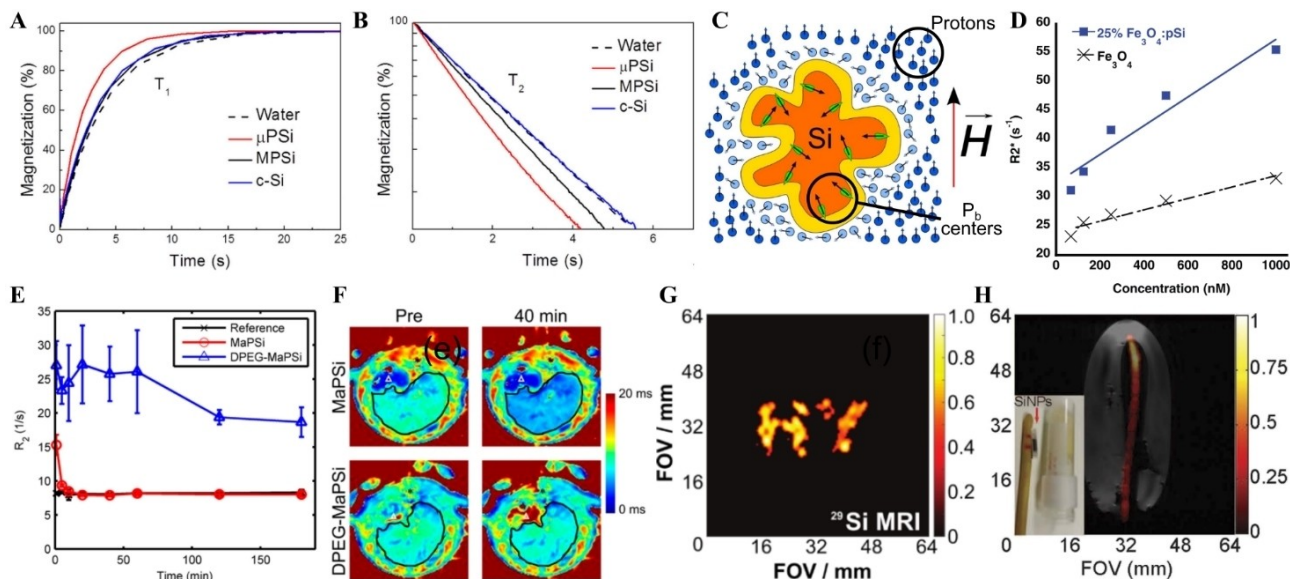## 2.2. Magnetic Resonance Imaging

Oxidized PSINPs without any special additives or surface modification can work as CAs for MRI by decreasing the T_1 and T_2 relaxation times (Figure 4A,B).[41] The decrease was correlated with the increase in the specific surface area (SSA), where the crystalline silicon had the lowest SSA, and microporous PSi

(pore size ≤ 2 nm) had the highest SSA. Alteration in the T_1 and T_2 relaxation times was attributed to the presence of paramagnetic defects called P_b centers (Figure 4C). These centers are dangling bonds of unbound Si atoms formed during oxidation of Si surfaces because of the lattice mismatch between Si and SiO_2. P_b centers are thus located close to the protons, and they can influence them through dipole-dipole interaction. This interaction, combined with the partial restriction of the movement of water molecules in the pores of PSi, decreases T_2 more significantly than T_1 (Figure 4A,B).[41a] Proton relaxation was further enhanced by increasing the concentration of PSINPs and using thermal annealing of PSINPs.[41a] The annealing resulted in the $\sim 10^{17}$ g^{-1} of P_b centers per mass of PSINPs and a transverse relaxivity rate R_2 of 0.5 g^{-1}s^{-1} or $\sim 10^{-2}$ mmol[Si]$^{-1}$s^{-1}.[41a] However, because of the small relaxivity rate ($\ll 4$–5.7 mmol[Gd]$^{-1}$ s^{-1} for conventional Gd^{3+} CAs), additional surface coatings are needed for biocompatibility.[42] Moreover, because of the difficulty of further increasing the number of P_b centers, the use of oxidized PSINPs is challenging for proton-based T_1- and T_2-weighted MRI.

To achieve high contrast in MRI, PSINPs were combined with Gd^{3+}-based CAs.[43] Interestingly, Gd^{3+}-based complexes demonstrated a significantly enhanced longitudinal relaxivity rate R_1 of up to ~ 24 mmol[Gd]$^{-1}$s^{-1} when loaded into PSINPs with 5–10 nm pores compared to the free CA value of 3.6–6.9 mmol[Gd]$^{-1}$s^{-1} in water.[44] The R_1 enhancement was attributed to the increase in both rotational and diffusion correlation times. The increase of rotational correlation time was governed by the restricted rotation of Gd^{3+}- complexes adsorbed or conjugated to the pore walls, while the diffusion correlation time increased because water diffusion in the pores was constrained. However, despite the promising enhancement *in vitro* and biodistribution studies,[44a] to our knowledge, Gd^{3+}

ChemMedChem

Review
doi.org/10.1002/cmdc.202200004

**Chemistry
Europe**
European Chemical
Societies Publishing

Figure 4. MRI of PSiNPs. A) Longitudinal and B) transverse proton magnetization of pure water (black dashed line) and aqueous suspensions of NPs (with a concentration of 1 g/l) prepared from bulk crystalline Si (c-Si, blue line), mesoporous Si (MPSi, black line), and microporous Si (μPSi, red line).[41b] Reproduced with permission from Ref. [41b]. Copyright 2018 AIP Publishing. C) Mechanism of MRI contrast of bare PSiNPs. Single PSiNPs (orange silicon core and yellow SiO_2 shell) induce fast relaxation of nearby protons (light blue circles) because of dipole–dipole interaction with paramagnetic (spin 1/2) dangling bonds in PSiNPs (green loops). The remote protons (dark blue circles) keep their magnetization in the direction of applied magnetic field H.[41a] Reproduced with permission from Ref. [41a]. Copyright 2015 AIP Publishing. D) MRI phantom experiments showing the weighted transverse relaxation time (R_2*) versus Fe concentration (nanomoles Fe per liter ultrapure water) for 25% (by mass Fe) Fe_3O_4-loaded PSiNPs (blue squares) and Fe_3O_4-containing PEG micelles (black x's).[45a] Reproduced with permission from Ref. [45a]. Copyright John Wiley and Sons. E) Measured T_2 relaxation rates (R_2, mean ± std, n = 3) for plasma samples taken from rats injected with NPs. The injected samples were 5% mannitol reference (black crosses), the PSiNPs with precipitated Fe_3O_4 NPs (MaPSi, red circles), and the DPEG-PSiNPs with Fe_3O_4 NPs (DPEG-MaPSi, blue triangles), both administered in 5% mannitol solution. F) MRI T_2* map of a rat liver before and 40 min after injection with 2 mL and 0.5 mg/mL of MaPSi or DPEG-MaPSiNPs. The liver is circled with a black line, the white triangle designates the cardiac part of the stomach, and the black asterisk shows the spinal cord. Subcutaneous fat is seen as having longer relaxation times. The four spots above the rat body were from the water-heated pad.[45b] Reproduced with permission from Ref. [45b]. Copyright 2016 American Chemical Society. G) Hyperpolarized [29]Si MRI with a shaped phantom taken 5 min after ~18 h polarization of PSiNPs. 45 mg of NPs were dispersed in PBS and placed into the phantom. The field of view (FOV) shows the spatial dimensions of the MRI scan.[47] Reproduced with permission from Ref. [47]. Copyright John Wiley and Sons. H) Real-time catheter tracking *in vivo* with co-registered [1]H: [29]Si MRI of hyperpolarized Si microparticles administered intravenously through a tail-vein catheter. The figure shows the movement of the catheter with Si NPs (inset) over the course of 3.2 seconds.[48b] Reproduced from Ref. [48b], open access.

-loaded PSiNPs have not yet been applied for T_1-weighted MRI *in vivo.*

Similar to Gd^{3+}, iron oxide NPs (SPIONs) were combined with PSi NPs.[45] Loading 9-nm Fe_3O_4 NPs into the PSi matrix enhanced the weighted transverse relaxivity rate R_2* from 333 mmol[Fe] $^{-1}s^{-1}$ to 556 mmol[Fe] $^{-1}s^{-1}$. This might be because of stronger magnetic interaction of closely located Fe_3O_4 confined in the pores (Figure 4D).[45a] Fe_3O_4 NPs also were precipitated directly in the pores of PSiNPs.[45b,c] These hybrid SPION-PSiNP complexes were used to study the dependence of systemic residence time for smartly designed PEG coatings.[45b] It was shown that dual coating with 0.5 kDa and 2 kDa PEG molecules increased the circulation half-life from 1 min for bare PSiNPs to 241 min for dual-PEG coated PSiNPs (Figure 4E). This is a necessary improvement for imaging other tissues besides the liver and spleen.

Finally, there have been substantial efforts to perform MRI with hyperpolarized [29]Si nuclei in bulk Si NPs,[46] PSiNPs,[47] and Si microparticles.[48] Hyperpolarization is the process of increasing the polarization of nuclei beyond thermal equilibrium.[49] Thus, each SiNP has large magnetization that can be detected without the need for a high magnetic field, and the imaging

can, in principle, be performed at a low field. This opens the possibilities of on-site diagnosis. To date, PSiNPs have been imaged only in a phantom (Figure 4G).[47] The first successful MRI *in vivo* included intratumorally, intravenously, rectally, and intraperitoneally injected Si microparticles[48a] and real-time catheter tracking (Figure 4H).[48b] However, there are still major technological challenges to be resolved before Si NPs can reach practical MRI applications. These challenges include expensive polarization equipment, long hyperpolarization time (~20 h), polarization loss during the transfer of NPs from the polarizer, and storage and redispersion of NPs into suspension before injection.

2.3. Nuclear Medicine Imaging
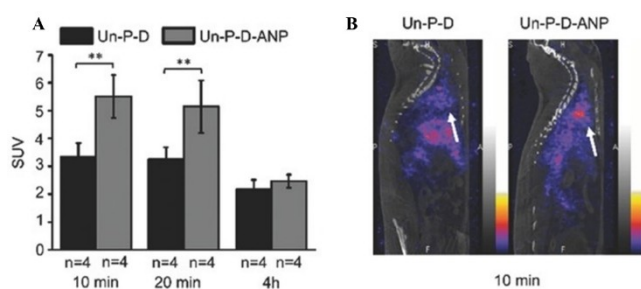
NMI methods have been extensively explored in the biomedical field. The NMI modality includes two main techniques: (1) PET detects gamma (γ) rays from the annihilation of electrons in the body and positrons from the decay of radionuclides. Today, several radionuclides (i.e., ^{68}Ga, [89]Zr, ^{64}Cu, ^{18}F, and [124]I) have been used in PET imaging. (2) SPECT detects gamma (γ) rays

during radionuclide decay.[21b] There are several SPECT radionuclides (i.e., ^{99m}Tc, ^{111}In, [198]Au, ^{123}I, and [186]Re) available. The most widely used SPECT radionuclide is ^{99m}Tc because of its easy production with a ^{99m}Tc generator. Because of the limited spatial resolution of NMI, it is common to integrate PET and SPECT with computed tomography (CT) to get a better 3-dimensional image of the object.[21a]

The traditional NMI CAs are radiolabeled molecules (i.e., proteins), which usually suffer from short circulation times in blood.[50] A variety of radiolabeled NPs have been considered advanced CAs for NMI. These radiolabeled NPs possess excellent cargo-loading capacity and facile surface functionalization methods being ideal NMI CAs for accurate cancer diagnosis and therapy to promote efficient treatment. Among various nanomaterials, PSi with excellent biocompatibility, easy surface functionalization, and high surface area is a promising radionuclide carrier material for NMI. In a typical example, Dave and coauthors labeled dual-PEGylated thermally oxidized porous silicon (DPEG-TOPSi) NPs with ^{111}In for SPECT/CT dual-modality imaging of 4T1 murine breast cancer. The blood radioactivity of mice treated with ^{111}In-DPEG-TOPSi was clearly higher than that of the control groups (^{111}In-TOPSi and free ^{111}In). This indicated the prolonged systemic circulation of the ^{111}In-DPEG-TOPSi group. However, it was difficult to visualize the 4T1 tumor from the SPECT/CT imaging because of a poor EPR effect in 4T1 tumors.[51]

Santos's group designed PEGylated and ^{111}In-labeled PSiNPs functionalized with atrial natriuretic peptide (ANP) for SPECT/CT imaging (Figure 5).[52] They compared the targeting of the NPs with and without ANP to the heart in vivo. Based on SPECT/CT imaging and the corresponding standardized uptake values, the ANP-functionalized PSiNPs indicated increased accumulation in the ischemic heart. The study also showed the improved ability of NPs loaded with trisubstituted-3,4,5 isoxazole to repair the endocardial layer. For the labeling process, the p-NH$_2$-B$_n$-DOTA-tetra(t-Bu-ester) served as the metal chelator for ^{111}In, and the as-prepared PSiNPs presented good colloidal and radiochemical stability because of the PEGylation. The work was a good

demonstration of the possibility of constructing a PSi-based nanoplatform by combining imaging and drug therapy.[52]

Besides SPECT/CT imaging, there are several PSi-based nanoplatforms for PET/CT imaging. For example, Outi and co-workers reported ^{18}F-tetrazine ([^{18}F])-labeled trans-cyclooctene (TCO)-PSiNPs based on inverse electron-demand Diels-Alder cycloaddition (IEDDA) reactions. The researchers determined that the molar ratio of TCO/[^{18}F] played an important role in vivo IEDDA labeling. Moreover, the isomerization of TCO groups or the formation of protein corona on the PSi surface may significantly affect the process of IEDDA, finally causing uncertainty in PET/CT imaging results.[53]

3. Summary and Outlook

Progress in the use of PSiNPs for optical imaging, NMI, and magnetic resonance imaging was reviewed. The unique advantages of PSi, such as good compatibility, intrinsic photoluminescence (PL), high surface area, and easy surface functionalization, may allow clinically applicable PSi-based contrast agents (CAs) for biomedical imaging.[18b,54] For example, the microsecond-level PL lifetime of PSi enables time-gated imaging for a significantly enhanced signal-to-noise ratio of PL imaging by eliminating the interference of tissue autofluorescence. The high surface area of PSi allows for the loading of different CAs for different imaging modalities. In addition, therapeutic agents can be simultaneously loaded into the PSi with the Cas. This integrates imaging and therapy to develop "all-in-one" theranostic nanoplatforms. Furthermore, surface functionalization of PSi empowers NPs to be smart platforms with cancer-targeted functions.

Despite the promising progress, several aspects need improvement to promote the development of PSiNPs in the future. First, a long-term and systematic study of the safety of PSiNPs is required. Studies have proven that PSi has good biocompatibility, but the reports have been based on short-term studies with small animals.[54a,55] Long-term and detailed safety profiles are required to convince administrative agencies and pharmaceutical investors. Second, personalized imaging CAs are required. Optical imaging, MRI, and NMI are versatile medical imaging modalities. Different persons have different biological environments and different developmental stages of their disease. Thus, there is a need to develop personalized imaging contrasts for intelligent biomedical imaging. The use of cell membrane coating is a feasible approach to developing personalized CAs. The cell membranes can be extracted from the diseased tissues of patients. The cell membrane-coated nanoparticles have excellent biocompatibility and homologous targeting for personalized biomedical imaging.[56] Third, a systematic design of PSi-based NPs should be considered for developing next-generation CAs. The NPs must overcome several biological barriers before reaching the targeting tissue. Different physicochemical parameters of PSi NPs affect their biological performance. The conventional "one variable at a time" method to optimize the design of NPs requires huge experimental resources and a long time to test the effect of

Figure 5. A) SPECT/CT image quantification of the standardized uptake values (SUVs) in the rat heart 10 min, 20 min, and 4 h after intravenous injection of NPs. B) Representative sagittal SPECT/CT images showing the biodistribution of the NPs 10 min after IV administration. Arrows indicate the location of the heart. Un–P–D: PEGylated and ^{111}In labeled PSi; Un-P–D-ANP: PEGylated and ^{111}In labeled PSi loaded with natriuretic peptide (ANP).[52] Adapted with permission from Ref. [52]. Copyright 2017, Wiley-VCH.

ChemMedChem

Review
doi.org/10.1002/cmdc.202200004

Chemistry
Europe
European Chemical
Societies Publishing

different parameters. This is not likely to be feasible in the development of NP-based imaging modalities. Fortunately, the development of advanced computational technologies, such as machine learning, has opened a new avenue for optimizing the design of NPs with low cost and high efficacy.[57] Thus, the use of a machine learning-assisted strategy will be a new trend to develop novel PSi-based imaging modalities.

Acknowledgements

Conflict of Interest

The authors declare no conflict of interest.

[1] E. A. Owens, M. Henary, G. El Fakhri, H. S. Choi, *Acc. Chem. Res.* **2016**, *49*, 1731–1740.

[2] a) Z. Zhang, F. L. Zhou, G. L. Davies, G. R. Williams, *View* **2021**, 20200134; b) S. S. Kelkar, T. M. Reineke, *Bioconjugate Chem.* **2011**, *22*, 1879–1903; c) J. H. Turner, *Cancer Biother. Radiopharm.* **2019**, *34*, 135–140.

[3] a) R. J. G. van Sloun, R. Cohen, Y. C. Eldar, *Proc. IEEE* **2020**, *108*, 11–29; b) A. Farhdi, M. G. Shapiro, *Science* **2019**, *365*, 1469–1475.

[4] a) W. Zhu, W. Ma, Y. Su, Z. Chen, X. Chen, Y. Ma, L. Bai, W. Xiao, T. Liu, H. Zhu, X. Liu, H. Liu, X. Liu, Y. M. Yang, *Light-Sci. Appl.* **2020**, *9*, 112; b) A. Sakdinawat, D. Attwood, *Nat. Photonics* **2010**, *4*, 840–848.

[5] a) E. Bombardieri, M. Maccauro, E. De Deckere, G. Savelli, A. Chiti, *Ann. Oncol.* **2001**, *12 Suppl 2*, S51–61; b) H. Schoder, Y. E. Erdi, S. M. Larson, H. W. Yeung, *Eur. J. Nucl. Med. Mol. Imaging* **2003**, *30*, 1419–1437; c) J. F. Gomes Marin, R. F. Nunes, A. M. Coutinho, E. C. Zaniboni, L. B. Costa, F. G. Barbosa, M. A. Queiroz, G. G. Cerri, C. A. Buchpiguel, *Radiographics* **2020**, *40*, 1715–1740.

[6] a) H. V. Nguyen, Q. Chen, J. T. Paletta, P. Harvey, Y. Jiang, H. Zhang, M. D. Boska, M. F. Ottaviani, A. Jasanoff, A. Rajca, J. A. Johnson, *ACS Cent. Sci.* **2017**, *3*, 800–811; b) F. H. Drost, D. Osses, D. Nieboer, C. H. Bangma, E. W. Steyerberg, M. J. Roobol, I. G. Schoots, *Eur. Urol.* **2020**, *77*, 78–94.

[7] Y. Wang, Y. Zhang, J. Wang, X. J. Liang, *Adv. Drug Delivery Rev.* **2019**, *143*, 161–176.

[8] T. F. Massoud, S. S. Gambhir, *Genes & Development, Vol. 17*, Old Spring Harbor Laboratory Press **2013**, 545–580.

[9] J. Tian, Y. Luo, L. Huang, Y. Feng, H. Ju, B. Y. Yu, *Biosens. Bioelectron.* **2016**, *80*, 519–524.

[10] C. Bharti, U. Nagaich, A. K. Pal, N. Gulati, *Int J Pharm Investig* **2015**, *5*, 124–133.

[11] a) M. L. Chen, Y. J. He, X. W. Chen, J. H. Wang, *Bioconjugate Chem.* **2013**, *24*, 387–397; b) N. Kohler, C. Sun, A. Fichtenholtz, J. Gunn, C. Fang, M. Zhang, *Small* **2006**, *2*, 785–792.

[12] a) M. A. Stuart, W. T. Huck, J. Genzer, M. Muller, C. Ober, M. Stamm, G. B. Sukhorukov, I. Szleifer, V. V. Tsukruk, M. Urban, F. Winnik, S. Zauscher, I. Luzinov, S. Minko, *Nat. Mater.* **2010**, *9*, 101–113; b) Z. R. Lu, F. Ye, A. Vaidya, *J. Controlled Release* **2007**, *122*, 269–277; c) X. Feng, F. Lv, L. Liu, H. Tang, C. Xing, Q. Yang, S. Wang, *ACS Appl. Mater. Interfaces* **2010**, *2*, 2429–2435.

[13] a) C. Yao, P. Wang, X. Li, X. Hu, J. Hou, L. Wang, F. Zhang, *Adv. Mater.* **2016**, *28*, 9341–9348; b) T. van der Geest, P. Laverman, J. M. Metselaar, G. Storm, O. C. Boerman, *Expert Opin. Drug Delivery* **2016**, *13*, 1231–1242.

[14] T. Nakamura, F. Sugihara, H. Matsushita, Y. Yoshioka, S. Mizukami, K. Kikuchi, *Chem. Sci.* **2015**, *6*, 1986–1990.

[15] a) T. K. Jain, J. Richey, M. Strand, D. L. Leslie-Pelecky, C. A. Flask, V. Labhasetwar, *Biomaterials* **2008**, *29*, 4012–4021; b) P. C. Liang, Y. C. Chen, C. F. Chiang, L. R. Mo, S. Y. Wei, W. Y. Hsieh, W. L. Lin, *Int. J. Nanomed.* **2016**, *11*, 2021–2037.

[16] a) C. F. Wang, E. M. Makila, M. H. Kaasalainen, M. V. Hagstrom, J. J. Salonen, J. T. Hirvonen, H. A. Santos, *Acta Biomater.* **2015**, *16*, 206–214; b) T. Tieu, M. Alba, R. Elnathan, A. Cifuentes-Rius, N. H. Voelcker, *Advanced Therapeutics* **2018**, *2*, 1800095; c) D. S. Karaman, M. P. Sarparanta, J. M. Rosenholm, A. J. Airaksinen, *Adv. Mater.* **2018**, *30*, e1703651; d) S. N. Jenie, B. Prieto-Simon, N. H. Voelcker, *Biosens. Bioelectron.* **2015**, *74*, 637–643; e) F. Zhang, A. Correia, E. Makila, W. Li, J. Salonen, J. J. Hirvonen, H. Zhang, H. A. Santos, *ACS Appl. Mater. Interfaces* **2017**, *9*, 10034–10046.

[17] a) A. Cifuentes-Rius, A. Ivask, E. Sporleder, I. Kaur, Y. Assan, S. Rao, D. Warther, C. A. Prestidge, J. O. Durand, N. H. Voelcker, *Small* **2017**, *13*; b) H. Alhmoud, B. Delalat, R. Elnathan, A. Cifuentes-Rius, A. Chaix, M.-L. Rogers, J.-O. Durand, N. H. Voelcker, *Adv. Funct. Mater.* **2015**, *25*, 1137–1145.

[18] a) J. Salonen, V.-P. Lehto, *Chem. Eng. J.* **2008**, *137*, 162–172; b) W. Xu, J. Rytkönen, S. Rönkkö, T. Nissinen, T. Kinnunen, M. Suvanto, A. Närvänen, V.-P. Lehto, *Chem. Mater.* **2014**, *26*, 6734–6742.

[19] J. Salonen, L. Laitinen, A. M. Kaukonen, J. Tuura, M. Bjorkqvist, T. Heikkila, K. Vaha-Heikkila, J. Hirvonen, V. P. Lehto, *J. Controlled Release* **2005**, *108*, 362–374.

[20] a) D. X. Zhang, C. Yoshikawa, N. G. Welch, P. Pasic, H. Thissen, N. H. Voelcker, *Sci. Rep.* **2019**, *9*, 1367; b) W. Xu, J. Riikonen, T. Nissinen, M. Suvanto, B. Li, F. Deng, V.-P. Lehto, *J. Phys. Chem.* **2012**, *116*, 22307–22314.

[21] a) J. Pellico, P. J. Gawne, T. M. d. Rosale, *Chem. Soc. Rev.* **2021**, *50*, 3355–3423; b) J. Ge, Q. Zhang, J. Zeng, Z. Gu, M. Gao, *Biomaterials* **2020**, *228*, 119553; c) H. A. Santos, L. M. Bimbo, B. Herranz, M.-A. Shahbazi, J. Hirvonen, J. Salonen, *J. Mater. Res.* **2012**, *28*, 152–164.

[22] G. D. Luker, K. E. Luker, *J. Nucl. Med.* **2008**, *49*, 1–4.

[23] B. R. Smith, S. S. Gambhir, *Chem. Rev.* **2017**, *117*, 901–986.

[24] S. A. Huettel, A. W. Song, G. McCarthy, *Functional magnetic resonance imaging, Vol. 1*, Sinauer Associates Sunderland, MA, **2004**.

[25] Z. Zhou, D. Li, H. Yang, Y. Zhu, S. Yang, *Dalton Trans.* **2011**, *40*, 11941–11944.

[26] M. Hamoudeh, M. A. Kamleh, R. Diab, H. Fessi, *Adv. Drug Delivery Rev.* **2008**, *60*, 1329–1346.

[27] C. Tu, X. Ma, A. House, S. M. Kauzlarich, A. Y. Louie, *ACS Med. Chem. Lett.* **2011**, *2*, 285–288.

[28] D. H. Li, C. L. Schreiber, B. D. Smith, *Angew. Chem. Int. Ed. Engl.* **2020**, *59*, 12154–12161.

[29] D. Liu, R. C. Huxford, W. Lin, *Angew. Chem. Int. Ed. Engl.* **2011**, *50*, 3696–3700.

[30] a) T. Kumeria, S. J. P. McInnes, S. Maher, A. Santos, *Expert Opin. Drug Delivery* **2017**, *14*, 1407–1422; b) D. J. Savage, X. Liu, S. A. Curley, M. Ferrari, R. E. Serda, *Curr. Opin. Pharmacol.* **2013**, *13*, 834–841; c) A. Chaix, K. Rajoua, V. Stojanovic, K. El Cheikh, E. Bouffard, A. Brocéro, M. Garcia, M. Maynadier, A. Morère, M. Gary-Bobo, F. Favier, J.-O. Durand, F. Cunin, *ChemNanoMat* **2018**, *4*, 343–347.

[31] N. Z. Knezevic, V. Stojanovic, A. Chaix, E. Bouffard, K. E. Cheikh, A. Morere, M. Maynadier, G. Lemercier, M. Garcia, M. Gary-Bobo, J. O. Durand, F. Cunin, *J. Mater. Chem. B* **2016**, *4*, 1337–1342.

[32] S. V. Zabotnov, A. V. Skobelkina, E. A. Sergeeva, D. A. Kurakina, A. V. Khilov, F. V. Kashaev, T. P. Kaminskaya, D. E. Presnov, P. D. Agrba, D. V. Shuleiko, P. K. Kashkarov, L. A. Golovan, M. Y. Kirillin, *Sensors (Basel)* **2020**, *20*.

[33] B. Xia, J. Li, J. Shi, Y. Zhang, Q. Zhang, Z. Chen, B. Wang, *ACS Biomater. Sci. Eng.* **2017**, *3*, 2579–2587.

[34] a) Y. Park, J. Yoo, M. H. Kang, W. Kwon, J. Joo, *J. Mater. Chem. B* **2019**, *7*, 6271–6292; b) E. Tasciotti, B. Godin, J. O. Martinez, C. Chiappini, R. Bhavane, X. Liu, M. Ferrari, *Mol. Imaging* **2011**, *10*, 7290.2011.00011.

[35] K. Cui, Y. Chang, P. Liu, L. Yang, T. Liu, Z. Zheng, Y. Guo, X. Ma, *ACS Sustainable Chem. Eng.* **2020**, *8*, 17439–17446.

[36] a) C. Schiattarella, R. Moretta, T. Defforge, G. Gautier, B. Della Ventura, M. Terracciano, C. Tortiglione, F. Fardella, P. Maddalena, L. De Stefano, R. Velotta, I. Rea, *J Biophotonics* **2020**, *13*, e202000272; b) G. H. Kim, G. Lee, M. H. Kang, K. Kim, Y. Jin, S. Beck, J. Cheon, J. Sung, J. Joo, *Faraday Discuss.* **2020**, *222*, 304–317; c) A. P. Mann, P. Scodeller, S. Hussain, J. Joo, E. Kwon, G. B. Braun, T. Molder, Z. G. She, V. R. Kotamraju, B. Ranscht, S. Krajewski, T. Teesalu, S. Bhatia, M. J. Sailor, E. Ruoslahti, *Nat.*

ChemMedChem

Review

doi.org/10.1002/cmdc.202200004

Chemistry Europe
European Chemical
Societies Publishing

Commun. **2016**, *7*, 11980; d) J. Wang, D. X. Ye, G. H. Liang, J. Chang, J. L. Kong, J. Y. Chen, *J. Mater. Chem. B* **2014**, *2*, 4338–4345.

[37] L. Gu, D. J. Hall, Z. Qin, E. Anglin, J. Joo, D. J. Mooney, S. B. Howell, M. J. Sailor, *Nat. Commun.* **2013**, *4*, 2326.

[38] J. Joo, M. J. Sailor, *ACS Nano* **2015**, *9*, 6233–6241.

[39] a) L. Hou, P. Ning, Y. Feng, Y. Ding, L. Bai, L. Li, H. Yu, X. Meng, *Anal. Chem.* **2018**, *90*, 7122–7126; b) P. Ning, W. Wang, M. Chen, Y. Feng, X. Meng, *Chin. Chem. Lett.* **2017**, *28*, 1943–1951.

[40] D. Kim, J. Kang, T. Wang, H. G. Ryu, J. M. Zuidema, J. Joo, M. Kim, Y. Huh, J. Jung, K. H. Ahn, K. H. Kim, M. J. Sailor, *Adv. Mater.* **2017**, *29*.

[41] a) M. B. Gongalsky, Y. V. Kargina, L. A. Osminkina, A. M. Perepukhov, M. V. Gulyaev, A. N. Vasiliev, Y. A. Pirogov, A. V. Maximychev, V. Y. Timoshenko, *Appl. Phys. Lett.* **2015**, *107*, 233702; b) Y. V. Kargina, M. B. Gongalsky, A. M. Perepukhov, A. A. Gippius, A. A. Minnekhanov, E. A. Zvereva, A. V. Maximychev, V. Y. Timoshenko, *J. Appl. Phys.* **2018**, *123*, 104302.

[42] S. Nakki, J. Rytkonen, T. Nissinen, C. Florea, J. Riikonen, P. Ek, H. Zhang, H. A. Santos, A. Narvanen, W. Xu, V. P. Lehto, *Acta Biomater.* **2015**, *13*, 207–215.

[43] S. Sinha, W. Y. Tong, N. H. Williamson, S. J. P. McInnes, S. Puttick, A. Cifuentes-Rius, R. Bhardwaj, S. E. Plush, N. H. Voelcker, *ACS Appl. Mater. Interfaces* **2017**, *9*, 42601–42611.

[44] a) A. Gizzatov, C. Stigliano, J. S. Ananta, R. Sethi, R. Xu, A. Guven, M. Ramirez, H. Shen, A. Sood, M. Ferrari, L. J. Wilson, X. Liu, P. Decuzzi, *Cancer Lett.* **2014**, *352*, 97–101; b) R. Sethi, J. S. Ananta, C. Karmonik, M. Zhong, S. H. Fung, X. Liu, K. Li, M. Ferrari, L. J. Wilson, P. Decuzzi, *Contrast Media Mol. Imaging* **2012**, *7*, 501–508.

[45] a) J. M. Kinsella, S. Ananda, J. S. Andrew, J. F. Grondek, M. P. Chien, M. Scadeng, N. C. Gianneschi, E. Ruoslahti, M. J. Sailor, *Adv. Mater.* **2011**, *23*, H248–253; b) T. Nissinen, S. Nakki, H. Laakso, D. Kuciauskas, A. Kaupinis, M. I. Kettunen, T. Liimatainen, M. Hyvonen, M. Valius, O. Grohn, V. P. Lehto, *ACS Appl. Mater. Interfaces* **2016**, *8*, 32723–32731; c) S. Nakki, J. T. Wang, J. Wu, L. Fan, J. Rantanen, T. Nissinen, M. I. Kettunen, M. Backholm, R. H. A. Ras, K. T. Al-Jamal, V. P. Lehto, W. Xu, *Int. J. Pharm.* **2019**, *554*, 327–336.

[46] a) W. Nicholas, H. Jingzhe, M. Z. Niki, L. R. L. Ganesh, E. V. David, G. M. David, R. Rajesha, P. Rebecca, K. S. Anil, B. Pratip, *J. Med. Imaging* **2016**, *3*, 1–9; b) S. Pudalakatti, J. S. Enriquez, C. McCowan, S. Ramezani, J. S. Davis, N. M. Zacharias, D. Bourgeois, P. E. Constantinou, D. A. Harrington, D. Carson, M. C. Farach-Carson, P. K. Bhattacharya, *Wiley Interdiscip. Rev.*

Nanomed. Nanobiotechnol. **2021**, *13*, e1722; c) J. Hu, N. Whiting, P. Bhattacharya, *J. Phys. Chem. C* **2018**, *122*, 10575–10581; d) G. Kwiatkowski, F. Jahnig, J. Steinhauser, P. Wespi, M. Ernst, S. Kozerke, *Sci. Rep.* **2017**, *7*, 7946.

[47] H. Seo, I. Choi, N. Whiting, J. Hu, Q. S. Luu, S. Pudakalakatti, C. McCowan, Y. Kim, N. Zacharias, S. Lee, P. Bhattacharya, Y. Lee, *ChemPhysChem* **2018**, *19*, 2143–2147.

[48] a) M. C. Cassidy, H. R. Chan, B. D. Ross, P. K. Bhattacharya, C. M. Marcus, *Nat. Nanotechnol.* **2013**, *8*, 363–368; b) N. Whiting, J. Hu, J. V. Shah, M. C. Cassidy, E. Cressman, N. Z. Millward, D. G. Menter, C. M. Marcus, P. K. Bhattacharya, *Sci. Rep.* **2015**, *5*, 12842.

[49] G. B. Furman, S. D. Goren, V. M. Meerovich, V. L. Sokolovsky, *J. Magn. Reson.* **2020**, *320*, 106847.

[50] M. L. James, S. S. Gambhir, *Physiol. Rev.* **2012**, *92*, 897–965.

[51] D. Lumen, S. Nakki, S. Imlimthan, E. Lambidis, M. Sarparanta, W. Xu, V. P. Lehto, A. J. Airaksinen, *Pharmaceutica* **2019**, *11*.

[52] M. P. Ferreira, S. Ranjan, S. Kinnunen, A. Correia, V. Talman, E. Mäkilä, B. Barrios-Lopez, M. Kemell, V. Balasubramanian, J. Salonen, *Small* **2017**, *13*, 1701276.

[53] O. Keinanen, E. M. Makila, R. Lindgren, H. Virtanen, H. Liljenback, V. Oikonen, M. Sarparanta, C. Molthoff, A. D. Windhorst, A. Roivainen, J. J. Salonen, A. J. Airaksinen, *ACS Omega* **2017**, *2*, 62–69.

[54] a) K. Tamarov, S. Nakki, W. Xu, V. P. Lehto, *J. Mater. Chem. B* **2018**, *6*, 3632–3649; b) W. Xu, J. Leskinen, J. Tick, E. Happonen, T. Tarvainen, V. P. Lehto, *ACS Appl. Mater. Interfaces* **2020**, *12*, 5456–5461.

[55] S. Näkki, J. T. Wang, J. Wu, L. Fan, J. Rantanen, T. Nissinen, M. I. Kettunen, M. Backholm, R. H. A. Ras, K. T. Al-Jamal, V. P. Lehto, W. Xu, *Int. J. Pharm.* **2019**, *554*, 327–336.

[56] L. Liu, X. Bai, M. V. Martikainen, A. Karlund, M. Roponen, W. Xu, G. Hu, E. Tasciotti, V. P. Lehto, *Nat. Commun.* **2021**, *12*, 5726.

[57] K. T. Butler, D. W. Davies, H. Cartwright, O. Isayev, A. Walsh, *Nature* **2018**, *559*, 547–555.